# A Comparison of Charge Transfer Efficiency Measurement Techniques on Proton Damaged n-Channel CCDs for the Hubble Space Telescope Wide-Field Camera 3

Augustyn Waczynski, Elizabeth J. Polidan, Paul W. Marshall, *Member, IEEE*, Robert A. Reed, *Member, IEEE*, Scott D. Johnson, Robert J. Hill, Gregory S. Delo, Edward J. Wassell, and Edward S. Cheng

*Abstract*—**We examine proton-damaged charge-coupled devices (CCDs) and compare the charge transfer efficiency (CTE) degradation using extended pixel edge response, first pixel response, and $^{55}$Fe X-ray measurements. CTEs measured on Marconi and Fairchild imaging sensors CCDs degrade similarly at all signal levels, though some of the Fairchild CCDs had a supplementary buried channel.**

*Index Terms*—**CTE, CTE noise, EEPR, EEV, FPR, minichannel, proton radiation damage, radiation testing, SBC, scientific CCD, WFC3.**

## I. INTRODUCTION

A DETAILED understanding of how proton exposure degrades charge-coupled device (CCD) performance is critical to evaluating the changing scientific capabilities of a space-based instrument over time. The Detector Characterization Laboratory and the Radiation Effects and Analysis Group of the NASA Goddard Space Flight Center have measured the radiation characteristics of the Hubble Space Telescope (HST) Wide Field Camera 3 (WFC3) CCD detectors. The early phase of this effort is based on similar work performed by the HST Advanced Camera for Surveys (ACS) team for detectors manufactured by SITe.

Significant degradation of the CCD performance due to radiation has been observed in previous HST instruments [1], [2]. Over time, the CCDs show reduced charge transfer efficiency (CTE), increased dark current, and an increased number of "hot pixels." The statistical nature of the CTE damage results in reduced photometric accuracy and increased noise. The impact on photometric accuracy has been widely studied [2]; however, CTE loss and related noise effects are not well understood and are the focus of this investigation.

The CCD total dose effects for the five-year WFC3 radiation environment are expected to be negligible since the low Earth orbit results in only a few hundred rads(Si) behind the heavy shielding approximately 1-in Al equivalent [3]. Under these conditions, CTE and dark current changes are believed to be due to proton-induced displacement damage [4]. In n-channel CCDs, phosphorus-vacancy defect (E-center) formation results in the introduction of charge traps distributed throughout the buried channel region [5]. Further discussions of the defect formation and behavior, as well as the use of proton energy dependent nonionizing energy loss (NIEL) to evaluate the damage process, can be found in [4], [6], and [7].

## II. EXPERIMENT APPROACH

Since displacement damage is proportional to the NIEL for a given proton energy, the total displacement damage is proportional to the integral over the product of the differential radiation spectrum (the spectrum behind the shield) and the corresponding NIEL. A proton beam with a single energy of 63.3 MeV was used to simulate the total displacement damage expected at the HST orbit altitude. This energy is especially relevant since it is close to the maximum of the different spectra modeled for WFC3 [3]. Using the proton beamline at the University of California (UC)-Davis Crocker Nuclear Laboratory, our test program used three cumulative fluence steps of $1 \times 10^9$, $2.5 \times 10^9$, and $5 \times 10^9$ protons/cm$^2$ to simulate performance after 1, 2.5, and 5 years, respectively, of on-orbit exposure. The dosimetry error was less than 10%.

Marconi Applied Technologies Ltd. (Marconi) was selected as the primary supplier of CCDs for the WFC3 project, but we also examined the possibility of an alternate source with a supplemental buried channel (SBC) implant from Fairchild Imaging Sensors (Fairchild, formerly Lockheed Martin). The main objective of this program was to determine the CTE degradation as a function of proton fluence. In addition, dark current and read noise were closely examined after each exposure. Since

A. Waczynski was with Global Science & Technology, NASA Goddard Space Flight Center, Greenbelt, MD 20770 USA (e-mail: aw@tophat.gsfc.nasa.gov). He is now with Dorsal Networks, Columbia, MD 21046 USA (e-mail: awaczynski@dorsalnetworks.com).

E. J. Polidan, S. D. Johnson, and G. S. Delo are with Global Science & Technology, NASA/Goddard Space Flight Center, Greenbelt, MD 20771 USA (e-mail: epolidan@tophat.gsfc.nasa.gov; johnson@tophat.gsfc.nasa.gov; greg@tophat.gsfc.nasa.gov).

P. W. Marshall is with NASA/Goddard Space Flight Center, Brookneal, VA 24528 USA (e-mail: pwmarshall@aol.com).

R. A. Reed and E. S. Cheng are with NASA/Goddard Space Flight Center, Greenbelt, MD 20771 USA (e-mail: Robert.A.Reed.@gsfc.nasa.gov; ec@cobi.gsfc.nasa.gov).

R. J. Hill and E. J. Wassell are with Raytheon ITSS, NASA/Goddard Space Flight Center, Greenbelt, MD 20771 USA (e-mail: hill@tophat.gsfc.nasa.gov; edward@tophat.gsfc.nasa.gov).

Publisher Item Identifier S 0018-9499(01)10528-9.

dark current and CTE are strong functions of temperature, and the WFC3 detector is to operate at $-83\,^{\circ}$C or colder, all measurements were carried out at $-80$, $-90$, and $-100\,^{\circ}$C to map the temperature range of interest. Due to thermal gradients in the cryostat, the temperature error may be as high as $+2\,^{\circ}$C.

The CTE was measured using three different methods: extended pixel edge response (EPER), first pixel response (FPR), and an X-ray source ($^{55}$Fe). It is expected that the CTE results may vary, depending on the method of measurement. A particular method may be more or less appropriate, depending on the intended application. The X-ray method allows absolute CTE measurement, which aids in laboratory-to-laboratory comparisons. It is widely cited and produces excellent results if CTE degradation is not too severe. Since the X-ray based CTE measurement methods are limited to the signal size fixed by the X-ray energy, and practical limits of single pixel absorption make measurements of charge packets of greater than approximately 6000 electrons difficult, photometric-based alternatives are necessary to assess the signal-level dependence of CTE degradation. The widely used EPER method relies on a flat field exposure and on overclocking the array to measure the deferred charge. It may produce too optimistic results. Where frame store architectures permit, FPR is an alternative method that assesses the charge missing from the leading edge of a flat field image [8], [9]. As X-ray and FPR allow measurement of absolute CTE, they are preferred for applications with low background.

As the CTE is a function of the trapping and emission time constants, it changes with clocking speed and also with the type of image. The type of image is important since traps that encounter charge in every transfer will remain filled, whereas traps that see many transfers between charge packets will be more likely to be empty [4]. We have explored the sensitivity of the X-ray method to the density of single X-ray photon events in an image by measuring CTE as a function of mean time between single photon events [delta time ($\Delta T$)] for a given clock rate. As the X-ray image density changes, we found that charge transfer inefficiency (1-CTE, or CTI) may vary significantly.

Since the CTE depends on temperature and the mean time between X-ray events in transfer, when quoting CTE numbers these test conditions should be specified to allow a fair comparison.

## III. TESTED DEVICES

Two CCD44s from Marconi and four Startracker CCDs from Fairchild were tested. The CCD44s are back-illuminated and have a $4096 \times 2048$ format with $15\,\mu m^2$ pixels and amplifiers at both ends of a single (2048 pixel) serial register. The image register has two sections (each being $2048 \times 2048$ pixels) and therefore can be used as a frame transfer device. The image can be read by either of the two amplifiers or by both simultaneously, with each amplifier reading half of the image. Almost all data were acquired using both amplifiers simultaneously (a so-called split mode of operation). These are noninverted mode operation (IMO) [nonmultiphase pinned (MPP)] devices. The CCDs were operated with two image phases inverted during exposure and one kept high for charge storage.

The Startracker CCDs have a $1024 \times 512$ format and are frame transfer devices with two serial shift registers and four amplifiers. Two of the four devices we tested had an SBC. The devices had a pixel size of 15 $\mu$m, with 12 $\mu$m channel width. The additional implant for SBC had a width of 3 $\mu$m [10]. Three of the four devices were previously irradiated at UC Davis: two of them with a fluence of $2.09 \times 10^9$ protons/cm$^2$ and one with $6.25 \times 10^9$ protons/cm$^2$. A fourth nonirradiated device was used as a reference.

## IV. EXPERIMENTAL DETAILS

The Marconi CCDs were irradiated at room temperature, without bias. Three radiation steps were spaced a few months apart, with full characterization of the detectors performed before and after each step. Data were collected within two weeks after each irradiation.

Since the clocking speed influences CTE results, we specify that all tests used a transfer rate of 50 000 pixels per second for the serial register and 8000 rows per second for the image register. When testing and comparing different format devices, one needs to ensure that the resident time under each clock gate is the same. We have chosen to maintain the serial register speed and to use the timing associated with the format of the largest detector for all devices tested, which is the format of the WFC3 detector.

Both Marconi and Startracker CCDs are three-phase devices. Classical timing is used. The signal is processed using correlated double sampling (CDS), with approximately 8 $\mu$s windows for "up" and "down" (dual slope) integration. In the serial register phases, one and two are pulsed at the beginning of the pixel time followed by an up integration sequence. When phase 3 is pulsing, two things occur: the last pixel charge is placed at the floating diffusion diode of the output amplifier, and for all other pixels in the serial register, the charge is placed under phase 1. The pixel sequence ends with integration down and a reset. Since up and down integration take 8 $\mu$s each and the duration of phase 2 is approximately 400 ns, the charge resident time under each serial phase is as follows: phase 1 is 9.2 $\mu$s, phase 2 is 0.4 $\mu$s, and phase 3 is 8.4 $\mu$s, resulting in a total pixel time of 18 $\mu$s. Serial register clocks have a rise time and fall time equal to 100 ns. Clock line impedance is controlled to maintain overshoots well below 50 mV. During exposure, charge is collected and stored under image phase 2. Consistently, phase 2 is kept high during serial register readout. As a result, the charge resident time under phase 2 is the longest and equal to 19.9 ms. Resident time for phase 1 and phase 3 is equal to 60 $\mu$s. To assure good CTE, a minimum phase overlap time must be met. We used an overlap time equal to 20 $\mu$s, well above the vendor-specified 10 $\mu$s, and verified CTE sensitivity to that parameter at the lowest test temperature. Further increase in overlap time did not make any difference in CTE performance. CTE was measured with the X-ray method for 10, 20, and 30 $\mu$s overlap times before irradiation and was found to be the same within error of measurement. We performed the same experiment on an irradiated device with similar results.

The EPER technique was used to determine CTE as a function of the signal intensity. CTE was measured over a range of signals extending from 10 e$^-$s per pixel to full well. A large parallel overscan (approximately 500 rows) was needed since

some residual amount of charge affected the CTE computation, and we noted the importance of accurate determination of the baseline for both the EPER and FPR measurements.

FPR measurements were performed over the same range of signal intensities (approximately 10 e⁻ per pixel to full well). In most cases, the same image files were used to calculate both EPER and FPR results. In this test, flat illumination was applied, and then the lower part of the image was flushed three times, effectively emptying all traps. Then, the whole image was read at normal parallel transfer rates. As a result, the first half of the image was just a baseline. The leading pixels of the effective image lost charge as they were shifted over empty traps in the flushed area.

CCD44 amplifiers are designed for high-speed low-noise readout. It should be noted that "read noise" here means the noise of the readout amplifier and does not include any dark or "hot" pixel contribution. (However, it includes a small contribution from electronics controller noise, making the reported value an upper limit.) Noise was measured for a 50-kHz readout speed with correlated double sampling implemented as an "up down" (dual slope) integrator [11].

All images were collected with a large overscan area, thus facilitating the calculation of read noise. All dark data were collected as full frame images (no binning) to preserve spatial resolution of hot pixels.

## V. ANALYTICAL APPROACH

FPR and EPER measure CTE by counting charge trapped during transfer. The amount of trapped charge is the most relevant way to characterize transfer property (CTE) for a given application. Trapped charge is measured on the leading edge (FPR) or in the trailing tail (EPER). In both cases, the type of traps (capture and emission time constants) and their respective densities determine the character of the leading edge or the tail and the amount of deferred signal for a given readout speed.

The recognized way to compute CTE with the FPR method is to calculate the missing charge in the first leading pixel and use it as a measure of the trapped charge. This is a good approximation for large signal levels and where the amount of trapped charge is a relatively small percentage of the signal. When trapping significantly reduces the first pixel charge packet, it occupies a smaller volume and does not engage all traps corresponding to its original level. The subsequent charge packets fill these traps. To account for a trapping corresponding to a given signal level, all charge missing from the leading edge should be counted, not just the first pixel. This is very evident given low signal levels and poor CTE, when all charge in the first pixel may be lost and significant charge is sometimes lost in the following pixels as well (see Fig. 1). To account for that, we have included the missing charge from all leading pixels in the calculation. A comparison of both methods is shown in Fig. 2. The single-pixel-based curve saturates at low signal levels since there is no more charge to be deferred, while the alternative method shows a progressive increase in CTI value, as expected for low signal levels. This is in agreement with the EPER results, plotted as a straight line.

In the EPER trailing edge, when long emission time constants are encountered, released charge may be spread over
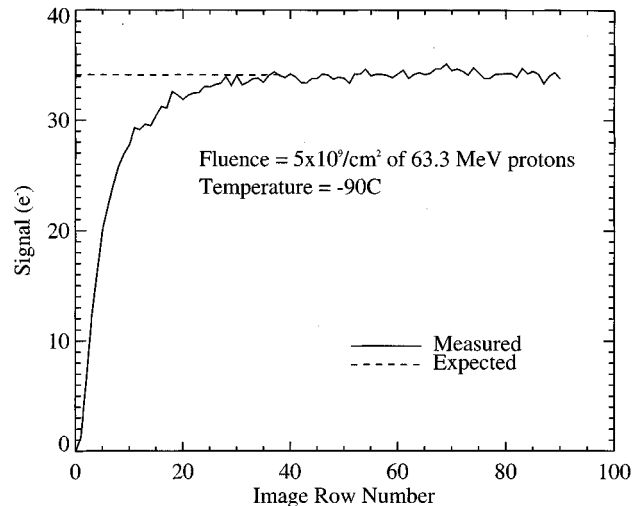


Fig. 1. The signal level of the first 90 rows of the image area after they were clocked out through an empty area of 2053 rows on the CCD. The expected and measured signal levels are shown. This reinforces the argument that using just the first pixel to calculate FPR CTI does not account for a large amount of charge lost in subsequent pixels.
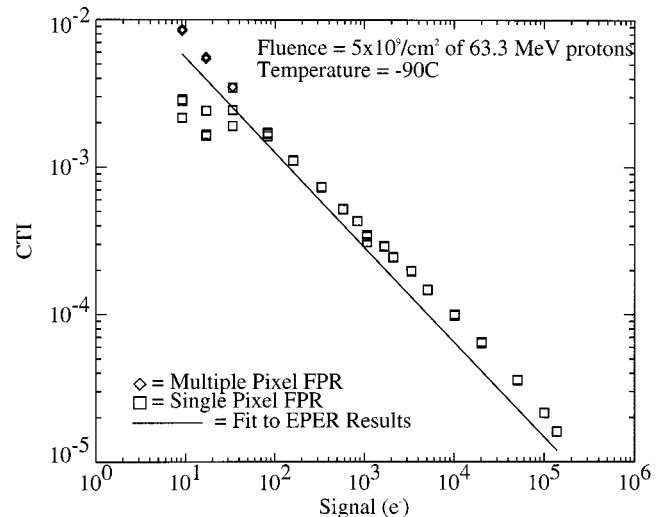


Fig. 2. Parallel CTI versus signal intensity. The CTI was derived with the FPR method using the first pixel only (squares) and then the first few pixels (diamonds). Using more than the first pixel brings the values at lower signal levels back in line with the rest of the curve. This adjusted curve agrees with EPER results and shows a more realistic CTI.

many pixels, even beyond the practical overscan. A small amount of charge per pixel makes it is difficult to recover from the noise. As a result, some of the reemitted charge is never realized and EPER CTE results tend to be on the optimistic side. Since in FPR we are looking for missing signal, we can account for all trapped charge. Considering that the area across which the charge is shifted is previously well cleaned and has all traps empty, FPR is the pessimistic or the worst case measure of CTE.

The X-ray method is similar to FPR in that CTE is calculated from the amount of lost signal. It has been the preferred method for many researchers because of its simplicity, reliability, and ease and accuracy of gain determination (the absolute charge of a single X-ray event allows for very convenient gain calibration
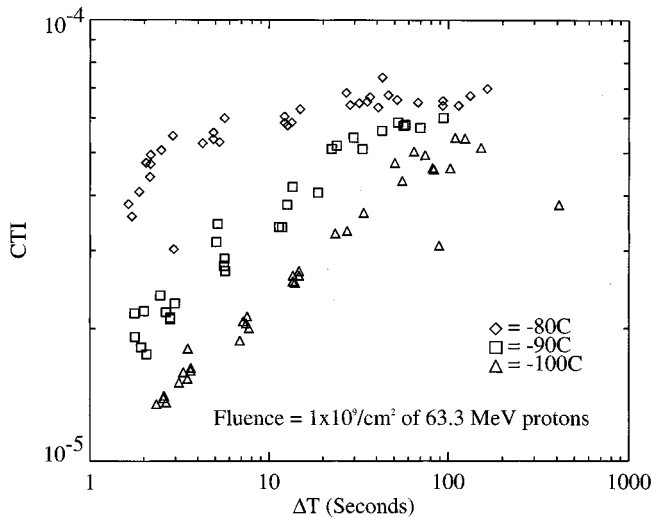
Fig. 3. This is the CTI measured by the X-ray method versus mean time between events ($\Delta T$) at three temperatures.



Fig. 4. Parallel CTI versus signal intensity at $-80\,^{\circ}$C. The CTI was calculated using the EPER and FPR methods. The single $^{55}$Fe point at an intensity of 1620 e$^{-}$ is overlaid to show the good agreement between all three methods.

compared with the photon transfer curve method). However, it is not free of the possibility of errors. The main problem is the mean time between clocked charge packets ($\Delta T$). When $\Delta T$ is comparable with the emission time constant, traps are not fully emptied. That makes the CTI value dependent on the density of the X-ray events in the image.

## VI. RESULTS

Careful control of conditions and methodical testing resulted in a good comparison between different methods and different devices. We show here a sampling of the copious amounts of data collected.

Temperature may have a significant influence on the CTE, especially after radiation damage, depending on the type of image. Special effort was undertaken to ensure that testing covered the signal intensity range and type of images expected in the WFC3 application. In the X-ray method, testing was extended to image densities corresponding to less than one event per 4000-pixel-long column. Fig. 3 shows the CTI of a device with one year's equivalent damage versus $\Delta T$ at three different temperatures. A decrease in temperature from $-80$ to $-100\,^{\circ}$C yields a decrease in CTI of up to a factor of three. The same magnitude of change can be observed for varying densities of X-ray events. At $-80\,^{\circ}$C, the trap emission time constant is short compared with the mean time between events ($\Delta T$) for most of the X-ray images. Traps become empty before the next event arrives and CTI is high and almost independent of $\Delta T$. At lower temperatures, the emission time constant becomes comparable with the longest $\Delta T$ tested, and a strong dependence on image density is observed. Fig. 3 demonstrates that a large error may result in comparing X-ray results with different image densities. Depending on the type of image ($\Delta T$), different conclusions about thermal dependence can be drawn: CTE for images with medium density is a strong function of temperature, while for sparsely populated images, CTE is almost independent of temperature. Our experience with CTE measurements confirms the conclusions of others [12], [13] that the X-ray method is a very reliable and convenient method of the CTE measurement.
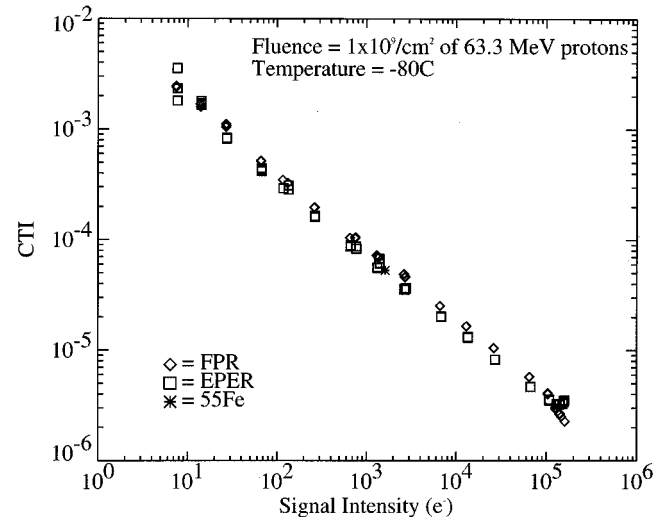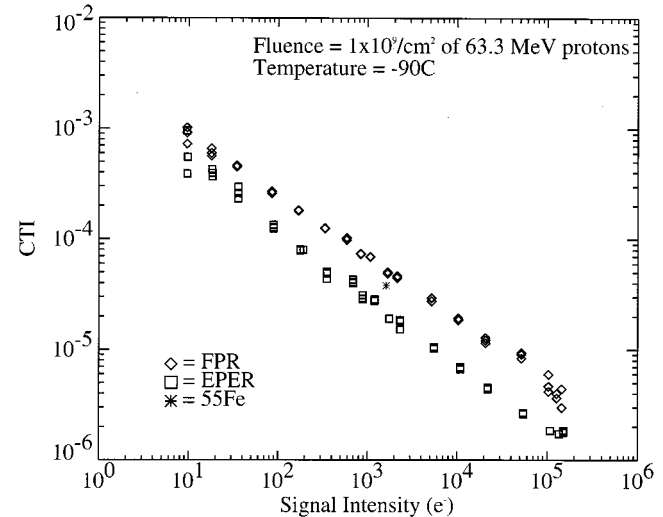


Fig. 5. This plot is a repeat of Fig. 4 at $-90\,^{\circ}$C. Here the EPER and FPR results are farther apart. The $^{55}$Fe point is closest to the FPR results.

However, when quoting CTE numbers, test conditions should be specified to allow a fair comparison.

### A. EPER, FPR, and X-Ray

EPER and FPR were used to examine CTE as a function of signal intensity. Ideally, both methods should yield identical results. As Fig. 4 shows, at $-80\,^{\circ}$C, EPER and FPR yielded practically the same results. Fig. 5 shows the same comparison for $-90\,^{\circ}$C. Here, the difference between EPER and FPR is noticeable. EPER shows lower CTI numbers, most likely due to the fact that not all deferred charge has been accounted for.

The X-ray data point is shown for an intensity of 1620 electrons in Figs. 4 and 5. The X-ray data point agrees in general with FPR, although it tends to be lower than that of FPR. One interpretation may be that CTI by X-ray varies significantly as a function of the mean time between X-ray events ($\Delta T$). The X-ray point here corresponds to a $\Delta T$ of 50 s. Considering that the longest time constant is around 1 s (see Table I), a 50-s $\Delta T$

| Temperature | | −80°C | −90°C | −100°C |
|---|---|---|---|---|
| Trap | Energy (eV) | Emission Time Constant (S) | | |
| A | 0.35 | 0.01 | 0.01 | 0.01 |
| B | 0.4 | 0.2 | 0.4 | 0.1 |
| C | 0.43 | 1. | 4. | 3. |
| D | 0.45 | 2.5 | 20.0 | 80+ |

should be enough to empty all traps before the arrival of the next charge packet. However, in Fig. 1, the slope of the curve implies a much longer time constant. The X-ray data point is still on the slope, and therefore it corresponds to the case where not all traps are fully depopulated for each charge packet.

Fig. 3 demonstrates that for low temperatures and relatively slow readout (50 kHz), parallel CTI depends on image density down to a single event per 4100-pixel column (which corresponds to a $\Delta T$ of greater than 100 s). This implies that for many practical cases, it is very difficult to design an EPER experiment where $\Delta T$ is high enough to produce a CTE equivalent to that of FPR (all traps empty). At low temperatures, in most cases the observed CTI will be reduced due to interactions between charge packets. Therefore, it is necessary to specify all relevant conditions such as temperature, clocking speed or resident times, and $\Delta T$ to compare CTE results.

Fig. 6 compares the measured CTI using the three techniques after exposure to $5 \times 10^9$ of 63.3 MeV protons/cm$^2$ (five-year equivalent). The agreement is quite good among the three methods. The EPER and FPR techniques both show the expected strong CTI dependence on signal size. It is expected that the CTI versus signal level is linear at higher signal levels and becomes nonlinear at lower signal levels [13]. Our parallel results reflect a curve that can be modeled by the equation CTI = constant − $x^m$, where $0.6 < m < 0.8$. One explanation could be that doping profiles in these devices are different [6].

Fig. 7 shows the serial CTI versus signal intensity for one year's equivalent damage at −80 °C. These data are only from EPER determination and X-ray because FPR measurements were not possible in the serial direction because of system constraints at that time. Serial CTI changes linearly for low signal and flattens out, as others have observed [13]. As expected, the serial CTE in a damaged device is an order of magnitude better than parallel CTE. This is believed to be due to much faster clocking speed, and thus shorter resident time, in the serial register [7]. Even so, at low signal levels, CTI is very high and may be a significant factor to consider in an application.

Fig. 8 shows that the CTE degradation was found to be linear with proton fluence, with an average parallel CTI slope of approximately $3.4 \times 10^{-5}$ per year of equivalent exposure. This number was measured with the X-ray method, at a temperature of −80 °C and a $\Delta T$ of approximately 50 s (which corresponds to two X-ray photons per column of 4100 pixels). Similar numbers were obtained with the EPER and FPR methods for the corresponding signal intensity of 1620 e$^-$/pixel.

## B. Emission Time Constant

We have attempted to identify traps by estimating their energy from the EPER data. For that, we used a combination of
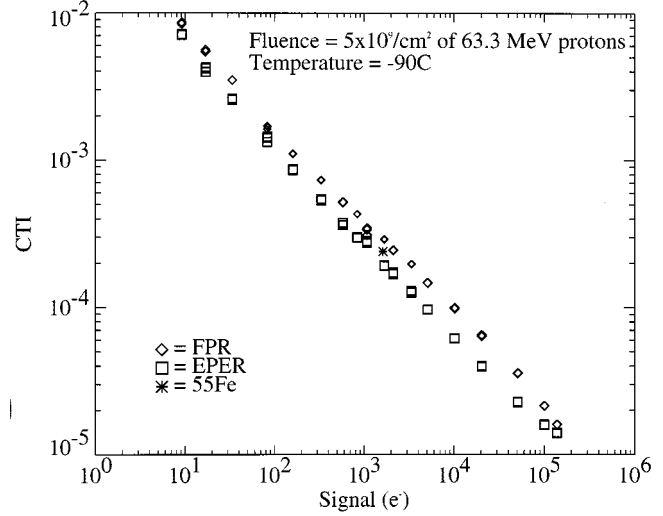


Fig. 6. This is a comparison of the parallel CTI results measured by the EPER, FPR, and X-ray methods for CCD44 with five equivalent years of damage. Note the good agreement between all three methods.
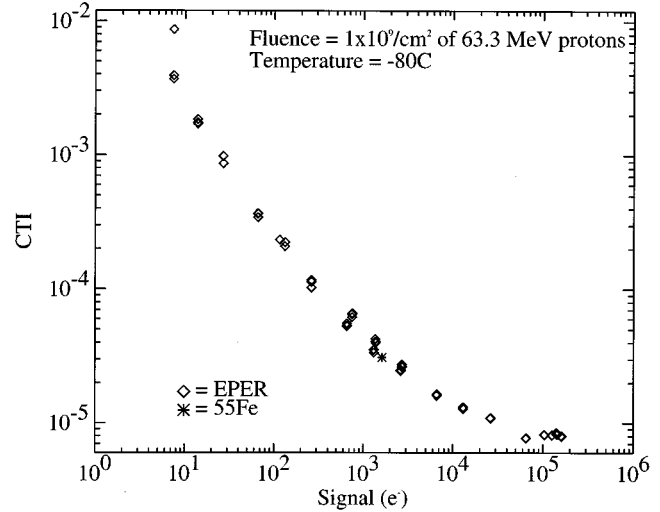


Fig. 7. This plot shows serial CTI versus signal intensity measured with the EPER method. The $^{55}$Fe point is overlaid to show the good agreement between the two methods.
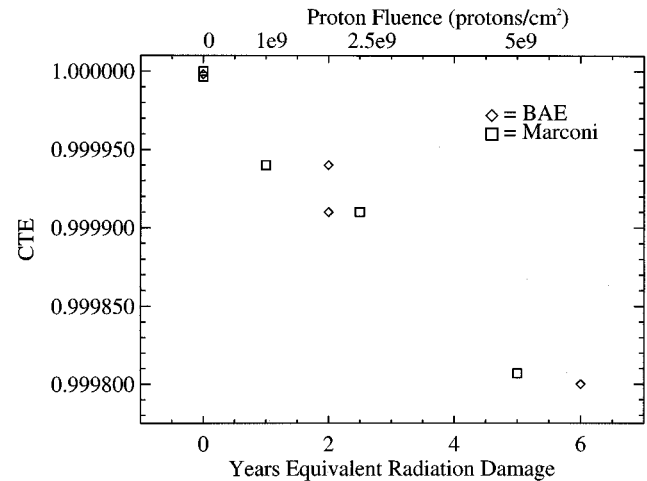


Fig. 8. This plot shows CTI as a function of proton fluence.

exponential curves to fit the EPER tails and to determine emission time constants. We used a parallel overscan of 200 to 900 rows, which corresponds to a time of 4 to 18 s. The results are shown in Table I.

A reasonably good fit to the EPER tail was achieved with three exponentials. The numbers at $-80\,^\circ$C show reasonable agreement with expectation. However, numbers for $-90$ and $-100\,^\circ$C are far off. We have concluded that we are not capturing all decays because of limited overscan size. An overscan of 18 s is sufficient to achieve a good fit for $-80\,^\circ$C; however, it appears to be insufficient for $-100\,^\circ$C. This is supported by the last row in Table I, with estimates of the time constant derived from X-ray data (see Fig. 3). As mentioned before, the X-ray data indicate existence of a trap with a time constant from 2.5 to 80+ s, depending on the temperature.

The second column shows energy computed from the data set at $-80\,^\circ$C, since it is believed to be the most reliable. The computation is based on a standard equation [6], using a cross-section of $3 \times 10^{15}$ [4].

### C. Read Noise

A noise of $<3$ e$^-$ rms was measured for both tested devices before radiation exposure and remained at this level after irradiation. Over the course of experiment, we occasionally observed higher numbers for read noise (in addition to special bias images for noise determination, noise was computed from parallel and horizontal overscans for each analyzed image). At this level, any change in experiment environment may affect noise results. However, low values of read noise were measured at each radiation step, and we can confidently state that up to highest irradiation level, we did not observe change in read noise.

Generally, it is expected that the flat band shift due to ionization charge trapped in the gate insulation dielectric will alter biasing of the output amplifier and may increase read noise. The total radiation dose for the highest exposure of $5 \times 10^9$ protons/cm$^2$ is less than 1 krad and is well within the vendor —specified radiation hardness of 10 krad [15]. For Marconi devices, the flat band shift corresponding to 1 krad dose is less than 15 mV [14], [15]. This amount of the bias change is too small to alter read noise performance.

### D. CTE Noise

We have demonstrated use of the FPR method to examine the average number of electrons trapped at a fixed damage level, signal level, and temperature, and we also use the FPR method to examine the distribution around that average. Recall that the FPR method relies on a flat field exposure to introduce a fixed charge packet that is then clocked along a column of 2053 pixels before being read out. In Fig. 9, we present histograms corresponding to charge packets at or near the leading edge of the flat field image.

In Fig. 9(a), the flat field illumination produced a very low signal level of about nine electrons. The top panel of Fig. 9(a) shows the leading pixel position. In a pristine imager, we would expect the histogram to be centered at a signal level of nine electrons with a distribution described by the read noise of approximately two electrons plus the photon shot noise of three electrons. Instead, we see the distribution centered around zero elec-
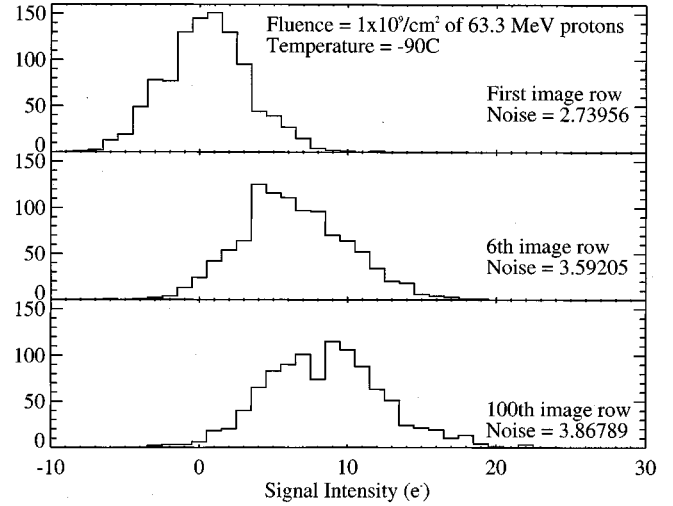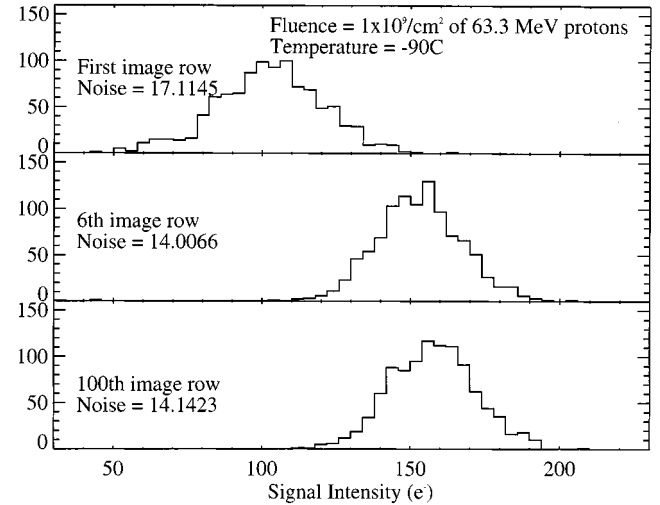


Fig. 9. This is a histogram of the charge distribution for the first few rows of the FPR image. (a) Shows the first image row, the sixth image row, and the hundredth image row for an image with a mean signal of ~9 e$^-$. (b) Shows the first image row, the sixth image row, and the hundredth image row for an image with a mean signal of ~160 e$^-$.

trons, and we conclude that all the charge from this packet has been trapped and the width is dominated by the amplifier read noise. The next panel of Fig. 9(a) shows the progression to the sixth row, where some charge appears and the width broadens. The hundredth row is well into the flat field region of the array and the width reflects the expected read noise and photon shot noise.

In Fig. 9(b), we have similar plots with a mean signal level of approximately 160 electrons. Note in the first row position that the mean is near 100 electrons but the width is over 17 electrons. This is greater than the read noise plus shot noise terms combined, and we conclude that the column-to-column variation in trap populations is a significant factor. At the sixth and hundredth row positions, this seems to have been "washed out" as the signal packet sizes increase to fill the available traps in a "fat zero" manner.

Fig. 10 shows measured versus expected noise for a few rows of the leading edge of an FPR image. The expected noise was
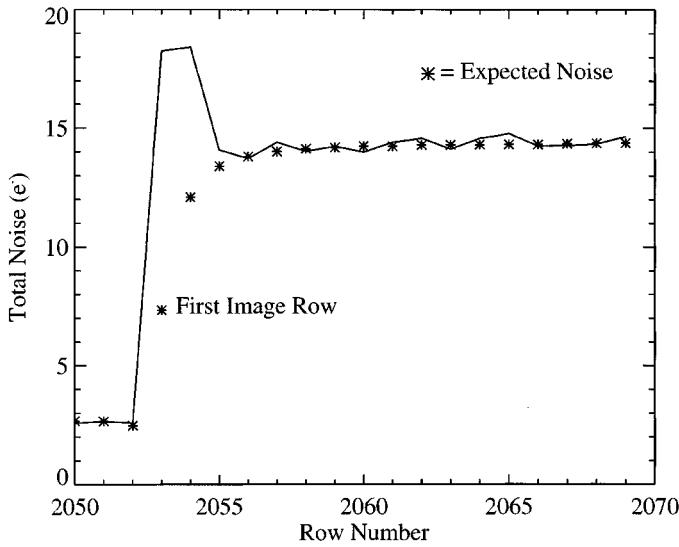
Fig. 10. This is a plot of observed and theoretical noise versus signal intensity for the first few rows of the FPR image.
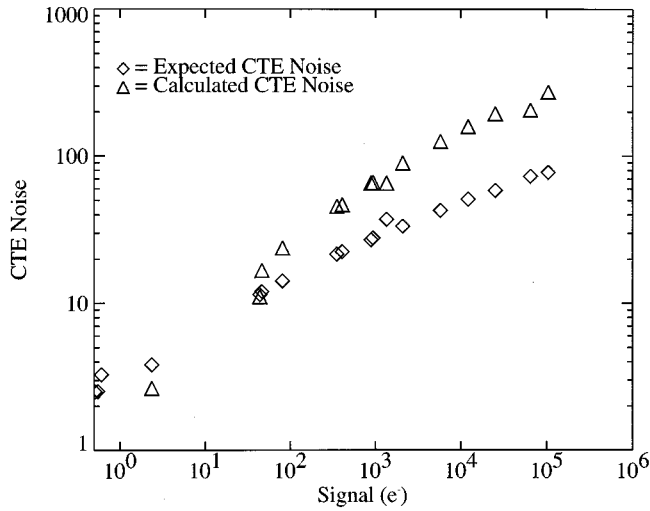


Fig. 11. This is the measured and expected CTE noise versus signal noise.



Fig. 12. CTI versus mean time between events ($\Delta T$) at $-80\,^{\circ}$C for SBC and non-SBC Startracker devices irradiated with $2 \times 10^9$ protons/cm$^2$.



Fig. 13. CTI by the EPER method for SBC Startracker versus signal intensity. No change in slope near the capacity level of the supplementary buried channel ($\sim 10\,000$ e$^-$) is observed.

calculated as an rms sum of the read noise, signal shot noise, and fixed pattern noise (due to image nonuniformity). Then, the difference was computed between the expected and the observed standard deviation. The differences for the first few leading rows (which have lost charge in the transfer) are significant. We consider this to be due to CTE caused noise. Looking at that as a function of signal intensity, we have concluded that "CTE noise" is proportional to the average signal level and degree of damage at this signal level, e.g., $\sigma(\text{CTI}) \sim \text{CTI} \times \text{mean(signal)}$, at least for the limited signal range.

In Fig. 11, we compare our data with the formula $\text{CTE\_noise} = (2 \times \text{CTI} \times N_p \times \text{signal})^{0.5}$, where $N_p$ is the number of pixel transfers [13], without good agreement. Measured noise is significantly higher than predicted by this equation. It increases overall noise for all signal levels by large amount. For a 2.5-year damaged device, its magnitude is comparable with signal shot noise. This behavior implies that CTE may cause a decrease in the signal-to-noise ratio at almost all signal levels, in addition to a signal-level change. This would
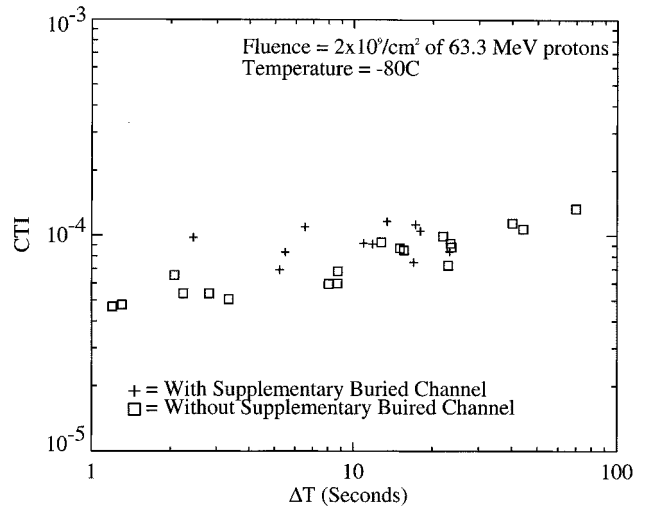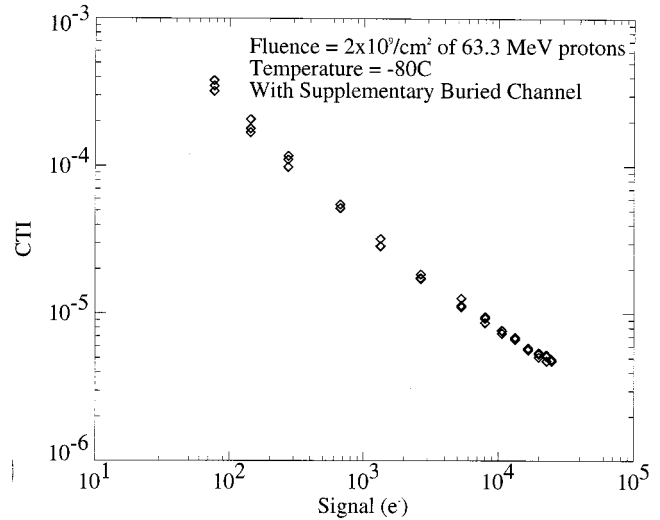
be the case even when an ideal CTE correction algorithm could be applied for reconstructing mean signal values.

CTE noise is a fixed pattern noise. We have shown this by correlating several images and showing good correlation for these rows where CTE noise was dominant. It is not related to the fixed pattern caused by response nonuniformity (PRNU). Nonuniformity can be corrected using flat field calibration. CTE noise does not have equivalent calibration procedures. As this is a fixed pattern noise, if it is understood, it can be corrected. Clearly, more work needs to be done in this area.

### E. Fairchild Versus Marconi

The irradiated Startracker devices show CTE similar to the Marconi CCDs. The two devices with lower fluence were of particular interest since one of them has an SBC in the parallel direction. It is commonly expected that the SBC would reduce CTE degradation, at least for low-level signals, because charge would be confined to the smaller volume of the SBC and would

encounter fewer traps. An effort was made to keep the same test conditions for Startracker devices as for the Marconi devices. Since the Startracker is a smaller device, we used a larger overscan in the horizontal direction to make the resident time for gates of the image register to be equal between both devices. We used the same test temperatures and readout speed. The Startracker devices have a frame transfer design that allows for measuring CTE with all three methods used for the Marconi devices. The results of the measurements are summarized in Figs. 12 and 13. Fig. 12 shows a comparison of the CTI for the CCD with an SBC and one without, both irradiated with a 2.5-year equivalent dose. The differences are insignificant. The same is seen when measuring with EPER and FPR. These plots (Fig. 13, for example) were examined for the presence of the slope change expected to occur at the signal point where the SBC capacity reaches saturation. In this case, the SBC is expected to have a capacity of 10 ke$^-$ [10]. Fig.13 shows no detection of slope change at that level. Although we were unable to detect evidence of the existence of the SBC, it should be noted that the above conclusions apply for CCDs at WFC3 operating conditions and may not be valid for different applications (e.g., different temperature and speed).

Fig. 8 showed CTI as a function of irradiation for all devices. Again, two of the Startracker SBC devices show degradation rates similar to other, non-SBC CCDs. The slope of the CTI versus proton fluence for Startracker devices is similar to Marconi devices.

## VII. CONCLUSION

We collected data at three different temperatures using three different methods of measurements (X-ray using an $^{55}$Fe source, EPER, and FPR). Care was taken to maintain the same experimental parameters and operating conditions for all devices involved. We demonstrated the dependence of CTE on X-ray photon density, signal intensity (EPER and FPR), and temperature. We have also investigated CTE-related noise effects. We have shown that CTE noise in radiation damaged CCDs is significant yet correctable. Further work is needed to fully understand CTE noise and develop corrective methods. The Startracker CCDs with and without a supplementary buried channel were found to have similar CTE degradation. The results of radiation testing of CCDs from the two manufacturers show reasonable agreement in the CTE data.

We confirmed the expectation that the read noise would not be affected by the amount of radiation expected in the HST environment.

## REFERENCES

[1] R. A. Kimble, P. Goudfrooij, and R. L. Gilliland, "Radiation damage effects on the CCD detector of the space telescope imaging spectrograph," in *Proc. SPIE*, vol. 4013, July 2000, pp. 532–544.

[2] B. Whitmore, I. Heyer, and S. Casertano, "Charge transfer efficiency of WFPC2," *Publications Astron. Society Pacific*, vol. 111, no. 766, pp. 1559–1576, Dec. 1999.

[3] J. Barth, NASA/Goddard Space Flight Center, private communication.

[4] C. J. Dale, P. Marshall, B. Cummings, L. Shamey, and A. Holland, "Displacement damage effects in mixed particle environments for shielding spacecraft CCDs," *IEEE Trans. Nucl. Sci.*, vol. 40, pp. 1628–1637, Dec. 1993.

[5] J. Janesick, G. Soli, T. Elliot, and S. Collins, "Effects of proton damage on charge coupled devices," in *Proc. SPIE*, vol. 1447, July 1991, pp. 87–108.

[6] T. Hardy, R. Murowinski, and M. J. Deen, "Charge transfer efficiency in proton damaged CCDs," *IEEE Trans. Nucl. Sci.*, vol. 45, pp. 154–163, Apr. 1998.

[7] G. R. Hopkinson, C. J. Dale, and P. W. Marshall, "Proton effects in charge-coupled devices," *IEEE Trans. Nucl. Sci.*, vol. 43, pp. 614–627, Apr. 1996.

[8] M. R. Jones, "Methods of measuring CTE," presented at the Space Telescope Science Institute CTE Workshop, Jan. 31–Feb. 1 2000.

[9] J. A. Gregory, B. E. Burke, and M. J. Cooper, "Solid state research," Lincoln Laboratory, Massachusetts Inst. of Technology, Quart. Tech. Rep. ESC-TR-92-149, Jan. 1993.

[10] G. R. Hopkinson, "Proton damage effects on $P$-channel CCDs," *IEEE Trans. Nucl. Sci.*, vol. 46, pp. 1790–1796, Dec. 1999.

[11] P. Vu, , July 3, 2001. Fairchild Imaging, Milpitas, CA, personal communication.

[12] R. Leach, "Operating a digital signal processor CCD camera under unix," *Publications Astron. Society Pacific*, vol. 8, pp. 171–187, Sept. 1989.

[13] M. Robbins, "The radiation damage performance of Marconi CCDs," Marconi Applied Technologies Tech. Note, Feb. 2000.

[14] J. Janesick, *Scientific Charge Coupled Devices*. Bellingham, WA: SPIE, 2001.

[15] "Marconi Applied Technologies, CCD44-82 back illuminated, high performance CCD sensors,", vol. 1, A1A-CCD44-82, May 2000. Back Illuminated Issue.